Comparative study of hydrotalcite-derived supported Pd$_2$Ga and PdZn intermetallic nanoparticles as methanol synthesis and methanol steam reforming catalysts

Antje Ota [a], Edward L. Kunkes [a], Igor Kasatkin [a], Elena Groppo [b], Davide Ferri [c], Beatriz Poceiro [d], Rufino M. Navarro Yerga [d], Malte Behrens [a,*]

[a] Fritz-Haber-Institute of the Max-Planck-Society, Department of Inorganic Chemistry, Faradayweg 4-6, D-14195 Berlin, Germany
[b] University of Torino, Department of Inorganic, Physical and Material Chemistry, NIS Centre of Excellence and INSTM, Via P. Giuria 7, I-10125 Torino, Italy
[c] Empa, Swiss Federal Laboratories for Materials Science and Technology, Laboratory for Solid State Chemistry and Catalysis, Ueberlandstrasse 129, CH-8600 Dübendorf, Switzerland
[d] Instituto de Catálisis y Petroleoquímica (CSIC), Grupo de Energía y Química sostenibles (EQS), C/Marie Curie, 2, 28049, Madrid, Spain

ARTICLE INFO

ABSTRACT

An effective and versatile synthetic approach to produce well-dispersed supported intermetallic nanoparticles is presented that allows a comparative study of the catalytic properties of different intermetallic phases while minimizing the influence of differences in preparation history. Supported PdZn, Pd$_2$Ga, and Pd catalysts were synthesized by reductive decomposition of ternary Hydrotalcite-like compounds obtained by co-precipitation from aqueous solutions. The precursors and resulting catalysts were characterized by HRTEM, XRD, XAS, and CO-IR spectroscopy. The Pd^{2+} cations were found to be at least partially incorporated into the cationic slabs of the precursor. Full incorporation was confirmed for the PdZnAl-Hydrotalcite-like precursor. After reduction of Ga- and Zn-containing precursors, the intermetallic compounds Pd$_2$Ga and PdZn were present in the form of nanoparticles with an average diameter of 6 nm or less. Tests of catalytic performance in methanol steam reforming and methanol synthesis from CO$_2$ have shown that the presence of Zn and Ga improves the selectivity to CO$_2$ and methanol, respectively. The catalysts containing intermetallic compounds were 100 and 200 times, respectively, more active for methanol synthesis than the monometallic Pd catalyst. The beneficial effect of Ga in the active phase was found to be more pronounced in methanol synthesis compared with steam reforming of methanol, which is likely related to insufficient stability of the reduced Ga species in the more oxidizing feed of the latter reaction. Although the intermetallic catalysts were in general less active than a Cu-/ZnO-based material prepared by a similar procedure, the marked changes in Pd reactivity upon formation of intermetallic compounds and to study the tunability of Pd-based catalysts for different reactions.

© 2012 Elsevier Inc. All rights reserved.

1. Introduction

Comparative studies of different (bi- or inter)metallic phases in nanostructured catalysts often suffer from limited comparability of the catalytic materials themselves as a result of differences in their preparation history. Application of the individually synthesis recipes that have been optimized for the best performance of a given catalyst system requires special and often unique conditions like presence of certain ligands, solvents, support materials, promoters, or thermal post-treatments. As a result, differences in composition, dispersion, homogeneity, or metal-support contacts may complicate the comparison of such nanocatalysts by convolution of extrinsic and intrinsic effects. Unsupported model catalysts are an alternative [1], but with the support often also the nanostructured

nature of the active phase and with it the easy relation to real powder catalysts has to be sacrificed. Recently, aerosol-derived alloy powders were presented as an elegant compromise and useful platform for studying intermetallic metal phase in MSR and CO oxidation on PdZn particles with a surface area of 6 m^2 g^{-1} [2].

While this approach successfully bridges the gap between model and real catalysts starting from the model side, we herein, present a synthetic approach to intermetallic catalysts that allows conserving the full complexity of supported nanocatalysts. At the same time, this method assures high comparability of different intermetallic compounds (IMCs) in a nanostructured form by application of a common and flexible synthesis protocol to minimize the role of different preparation history. This is achieved using a facile aqueous co-precipitation technique to prepare Hydrotalcite-like compounds (HTlc) with different elemental combinations as well-defined platform precursor materials for intermetallic compounds.
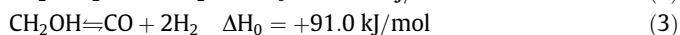
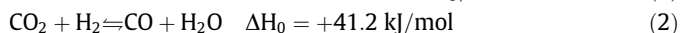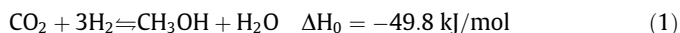* Corresponding author. Fax: +49 30 8413 4405.
E-mail address: behrens@fhi-berlin.mpg.de (M. Behrens).

The advantage of this precursor material is that divalent and trivalent cations are uniformly distributed in slabs of edge-sharing MO_6 octahedra that allow a close interaction of all metal cations, which is thought to be prerequisite to the uniform formation of IMCs [3]. HTlcs exhibit the general composition $\left(M1^{II}, M2^{II}\right)_{1-x}$ $M3_x^{III}(OH)_2(CO_3)_{x/2} \cdot mH_2O$ ($0.25 \leqslant x \leqslant 0.33$) and a huge flexibility of reducible and non-reducible metal cations that can be incorporated into the structure, for example, $M^{II} = Mg^{2+}$, Mn^{2+}, Co^{2+}, Ni^{2+}, Cu^{2+}, Zn^{2+} and $M^{III} = Al^{3+}$, Ga^{3+}, Fe^{3+}, Cr^{3+} [4]. This flexibility makes a large number of element combinations accessible rendering HTlc a platform precursor for many IMC systems. In this work, we use the HTlc precursor approach to compare the role of different Pd-based IMCs. We used Pd^{2+} as $M1^{II}$ and added reducible species, Zn^{2+} and Ga^{3+} at the $M2^{II}$ and M^{III} sites, respectively, to obtain the IMCs PdZn and Pd_2Ga. It is noted that due to the charge distribution the formed IMCs are sometimes denoted as ZnPd and $GaPd_2$. Here, we use in the field of catalysis more common form PdZn and Pd_2Ga for consistency with previous work.

We have shown recently [5] that Pd_2Ga nanoparticles supported on an oxide matrix of MgO and $MgGa_2O_4$ can be obtained by this synthetic approach and reported on their hydrogenation properties. This method presents an efficient alternative to previously used top-down methods, such as etching or milling of materials obtained from high temperature melt synthesis, used previously to synthesize this material [6]. In addition to catalyst synthesis and characterization data from a variety of complementary techniques (XRD, BET, TPR, SEM, TEM, FTIR, and XAFS), we also present catalytic performance data in two reactions involving methanol, namely its synthesis from CO_2 and methanol steam reforming (MSR) to correlate structural with catalytic properties.

Methanol has been proposed as a promising energy storage molecule for portable applications such as direct methanol fuel cells, as well as fuel for automobile internal combustion engines [7]. Additionally, methanol has been proposed as hydrogen storage medium [8], whose gravimetric hydrogen density exceeds that of compressed and even that of liquid hydrogen. Furthermore, the use of CO_2 as a carbon source for methanol synthesis enables the simultaneous reduction in emissions of this greenhouse gas [7].

Methanol synthesis from CO_2 (Reaction (1)) and its reverse reaction, methanol steam reforming (MSR) comprise a class of reactions critical to the application of methanol as an efficient energy carrier.

$$CO_2 + 3H_2 \rightleftharpoons CH_3OH + H_2O \quad \Delta H_0 = -49.8 \text{ kJ/mol} \tag{1}$$
$$CO_2 + H_2 \rightleftharpoons CO + H_2O \quad \Delta H_0 = +41.2 \text{ kJ/mol} \tag{2}$$
$$CH_2OH \rightleftharpoons CO + 2H_2 \quad \Delta H_0 = +91.0 \text{ kJ/mol} \tag{3}$$

Both reactions are currently carried out at similar temperatures (523–603 K) on Cu/ZnO-based catalysts. While MSR is not thermodynamically limited and is carried out at atmospheric pressure, methanol synthesis requires high pressures (30–100 bar) and lower operating temperatures due to unfavorable thermodynamics [9]. Reverse water gas shift (rWGS, Reaction (2)) is a side reaction to methanol synthesis and thus diminishes selectivity. In MSR, methanol decomposition (Reaction (3)) as well as rWGS are undesired side reactions and yield CO-a poison for fuel cell electrodes. The rates of both undesired reactions can be thermodynamically hindered by operating at lower temperatures. Lower temperature operation and low selectivity to rWGS or decomposition thus remain the driving forces behind the development and optimization of methanol catalysts [9].

The current state of the industrial Cu/ZnO catalysts are well suited to stationary operation, however suffer from pyrophoricity, sintering with long reaction times, and instability to changes in reaction conditions [10]. These shortcomings make Cu-based

catalysts unsuitable for portable applications. To that end, Pd supported on reducible oxides such as ZnO, In_2O_3, and Ga_2O_3 has shown favorable reactivity similar to that of Cu-based catalysts for both methanol synthesis and MSR [11], whereas Pd supported on non-reducible supports has been shown to be selective to rWGS and methanol decomposition. Additionally, Pd-based catalysts have also shown good long-term stability and resistance to sintering. The alteration of the properties of Pd was attributed to the formation of the IMCs Pd_2Ga [12] and PdZn [11a,13] upon partial reduction in the support components rendering these systems ideal test cases for studying the potential of the HTlc precursor approach for IMC catalysts synthesis.

2. Experimental

2.1. Synthesis conditions

Ternary palladium containing and binary Pd-free *PdMgAl*, *PdMgGa*, *PdZnAl*, *MgGa*, *ZnAl*, and *MgAl* HTlc with M^{2+}/M^{3+} molar ratios of 70:30 were synthesized by co-precipitation. The nominal composition of all Pd-M^{2+}–M^{3+} samples was set to 1:69:30. A mixed aqueous metal nitrate ($[Pd^{2+}] + [M^{2+}] + [M^{3+}] = 0.2$ M) solution and 0.345 M basic precipitating agent solution were co-fed at pH = 8.5. For *MgGa* and *MgAl*, HTlc precursors pure sodium carbonate solution and a precipitation temperature of 328 K were used, whereas in case of *PdZnAl* HTlc a mixture of sodium carbonate (0.3 M) and sodium hydroxide (0.045 M) and a temperature of 298 K has been applied in order to obtain an homogeneous precursor sample. During precipitation, both solutions were added simultaneously dropwise into a 2-L precipitation reactor (Mettler-Toledo LabMax). The nitrate solution was automatically pumped with a constant dosing rate, and the basic solution was added to maintain a constant pH of 8.5. After completion of addition, the mixture was aged for 1 h at the same temperatures applied during synthesis. The precipitate was filtered and washed twice with warm deionized water in order to remove the nitrate and sodium ions and obtain a conductivity of the filtrate lower than 0.2 mS/cm. The solid was dried for 12 h at 353 K in air. After drying, a one-step decomposition–reduction in 5 vol% H_2/Ar (2 K/min) was performed at the temperatures extracted from H_2-TPR experiments that yielded in the intermetallic phases and in metallic Pd in case of the *PdMgAl* HTlc precursor. A reduction temperature of 523 K was applied for the *PdMgAl* and *PdZnAl* system, whereas a reduction of 773 K is needed to obtain Pd_2Ga intermetallic particles.

A HTlc-based *CuZnAl* catalyst was prepared as described previously [14] and was used as reference material for the catalytic test in methanol synthesis. Additional details about the synthesis conditions of the *CuZnAl* HTlc precursor and the synthesis protocols of the Pd-based HTlc are given in the supplementary information (Fig. S1).

2.2. Characterization

X-ray diffraction. XRD patterns of the HTlc precursor and its decomposition products were recorded on a STOE Stadi P diffractometer in transmission geometry using Cu $K\alpha_1$ radiation, a primary Ge monochromator, and a 3° linear position sensitive detector.

Specific surface area determination. Specific surface areas (SSA) of the precursors and reduced compounds were determined by N_2 adsorption–desorption measurements at 77 K by employing the BET method (Autosorb-1C, Quantachrome). Prior to N_2 adsorption, the sample was outgassed at 353 K/423 K (precursor sample/reduced catalyst, respectively) to desorb moisture from the surface and pores.

Chemical analysis. About 5 mg was exactly weighted in and dissolved in 2 ml of aqua regia. The solutions were transferred and filled up in 50-ml volumetric flasks. The content of the metals were determined with ICP-OES (Vista RL, Varian) after matrix-matched calibration.

Temperature-programmed reduction. The TPR experiments were performed in a fixed-bed reactor using 400 mg of precursor (100–250 μm sieve fraction). *PdMgGa* and *PdMgAl* precursors were reduced in 5 vol% H_2 in Argon (100 ml/min) with a heating rate of 2 K/min up to a sample temperature of 773 K. The temperature was kept constant for 4 h. The *PdZnAl* precursor was heated to 1073 K (2 K/min). The hydrogen consumption was monitored with a thermal conductivity detector.

X-ray absorption fine structure. XAFS data were collected in the XANES (X-ray absorption near edge fine structure) and EXAFS (Extended X-ray absorption fine structure) regions at the Pd K edge (24.350 keV) were carried out at the Super-XAS beamline of the Swiss Light Source (Villigen, Switzerland) in the transmission mode, using ionization chambers as detectors and a Si(3 1 1) Quick EXAFS monochromator. A Pd foil placed between the second and third ionization chamber was measured simultaneously as an internal reference. In situ XANES measurements during hydrogen TPR were performed in transmission mode, using a 3-mm capillary reactor cell (Hilgenberg). The precursor (63–100 μm, 30 mg) was filled into the capillary between quartz wool plugs. The cell was connected to a gas manifold. The cell was convectively heated by means of an air blower. Spectra were collected during the reduction in 5 vol% H_2/N_2 (100 ml/min) in the temperature range of 303–773 K. For in situ MSR experiments, an HPLC pump was used to introduce 0.02 ml/min of a 1:1 M ratio methanol water solution into an SiC filled evaporator at 120 °C, where the vapor was diluted with 100 ml/min (STP) of He. The vapor sent to the reaction cell via heated lines, and the reactor outlet gas composition was monitored by MS. Data reduction was performed using the Athena 0.8.056 software package.

Fourier-transformed infrared absorption spectroscopy of CO. In situ experiments were carried out in a custom built quartz cell equipped with KBr windows allowing sample activation and successive measurements in the 292–823 K temperature range, at pressures from 10^{-4} to 760 Torr. The catalysts were pressed into self-supporting pellets and activated in the same cell used for the measurement. The thermal treatments were performed either in dynamic vacuum or under static conditions (no flux), according to procedures discussed below. In situ FTIR spectra on the investigated catalysts were recorded at a resolution of 2 cm^{-1} on a Nicolet 6700 instrument, in transmission mode. *PdZnAl* and *PdMgAl* HTlc precursors were outgassed in dynamic vacuum up to 523 K for several hours (until the pressure reached values below 10^{-4} Torr), followed by reduction in H_2 gas (2 cycles of 30 min, P_{H2} = 100 Torr). H_2 was removed from the cell at the same temperature, and the sample was allowed to reach room temperature in dynamic vacuum. PdGaMg HTlc precursor was outgassed in dynamic vacuum up to 823 K for several hours (until the pressure reached values below 10–4 mbar), followed by reduction in H_2 gas (4 cycles of 1 h, P_{H2} = 100 Torr). H_2 was removed from the cell at the same temperature, and the sample was allowed to reach room temperature in dynamic vacuum.

Scanning electron microscopy. SEM images were acquired with a Hitachi S4800 FEG microscope equipped with an EDS system (EDAX) for elemental analysis. The samples were loosely dispersed on a conductive carbon tape to preserve the as-prepared morphology as much as possible. SEM images were acquired at low accelerating voltage, that is, 1.5 kV, while EDX spectra were acquired at an accelerating voltage of 15 kV.

Electron microscopy. HRTEM images were acquired using a FEI TITAN microscope, equipped with a field emission gun (FEG) and operated at 300 kV. With computer-assisted correction and alignment, the value of the spherical aberration constant C_s was kept below 100 nm in the present experiments. Selected areas of the high-resolution images have been Fourier transformed to obtain Power spectra, and the lattice distances and angles were measured for phase identification (accuracy ±1% and ±0.5°, respectively). Metal dispersions for Pd-based catalysts were obtained by $D = 1.1/d$, where d is the average particle size determined by TEM neglecting the partial embedment of nanoparticles that reduces the availability of active sites. An estimate of the number of surface metal sites was calculated from this dispersion and the palladium loading, assuming complete accessibility of the surface to the gas phase. For bimetallic nanoparticles, incorporation of second metal (Zn or Ga) was assumed stoichiometric according to PdZn and Pd_2Ga.

2.3. Catalytic performance

2.3.1. Methanol synthesis from CO_2

Methanol synthesis experiments were carried out in a stainless steel fixed-bed flow reactor. 400 mg (100–200 μm) of HTlc precursor was mixed with 2 g of crushed SiO_2 chips and loaded into a 10 mm I.D. stainless steel reactor tube. Gas flows were controlled and monitored with analog mass flow controllers (Brooks 5850A).

The *PdZnAl* and *PdMgAl* HTlc precursors were reduced in situ at 523 K (2 K/min) for 2 h in 100 ml/min (STP) of 20 vol% H_2 in He. The *PdMgGa* HTlc precursor was reduced at 773 K (2 K/min) for 5 h in the same H_2/He mixture. Upon completion of the reduction, the reactor was cooled to 523 K, a 3:1 H_2/CO_2 mixture (100 ml/min) containing 4 vol% Ar (as internal standard) was introduced into the reactor, and the pressure was raised to 30 bar by means of a back-pressure regulator (Tescom). The back-pressure regulator and all high-pressure line were heated to 423 K to avoid condensation of water and methanol, and all low-pressure lines downstream of the back-pressure regulator were heated to 393 K. Online analysis of products was performed with a GC (Agilent 6890) equipped with a J&W scientific Haysep Q Column and a TCD for analysis of non-condensable gases and a Agilent DB1 column interfaced to an FID for analysis of methanol. Methanol and CO were the main products observed, along with traces (less than 0.1% selectivity) of methane. After the start of the reaction, the catalysts were allowed to stabilize for 20 h time-on-stream at 523 K. After this period, the activation energies of methanol synthesis and rWGS were measured in the temperature range of 463–548 K, with 4 h allowed for each temperature point. Conversions of CO_2 were below 3% insuring the absence of thermodynamic artifacts.

2.3.2. Methanol steam reforming

Methanol steam reforming (MSR) reaction was conducted using a fixed-bed flow reactor at 523 K and atmospheric pressure. Activity tests were performed using 0.125 g of HTlc precursor diluted with SiC at volume ratio of 3:1 to avoid adverse thermal effects. Catalyst bed was placed in a 6 mm I.D. quartz tubular reactor with a coaxially centered thermocouple. Prior to reaction, the *PdZnAl* and *PdMgAl* HTlc precursors were reduced in situ at 523 K (2 K/min) for 4 h in 60 cm^3 (STP) of 5 vol% H_2 in N_2. The *PdMgGa* HTlc precursor was reduced at 823 K (2 K/min) for 4 h in the same H_2/N_2 mixture. The pretreating gases were flushed from the reactor with N_2 before admission of methanol–water–nitrogen reaction mixtures. Methanol and water mixture was supplied into a preheater by means of a liquid pump (Becton–Dickinson) before their mixture with nitrogen carrier supplied by Brooks model 5850E mass flow controller. For MSR reaction, the reactants were introduced into the reactor in the molar ratio H_2O/CH_3OH = 1.0. In the MSR tests, the total flow rate was kept at 26 ml/min (STP), and the methanol concentration in the feed gas mixture was fixed at

28.4 vol% to avoid thermal effects derived from the high endothermicity of the reaction.

The reaction products were analyzed on line by GC with TCD (HP 6890 GC) equipped with CP-Porabond Q (CO_2, water, methanol, formaldehyde, methyl formate, and dimethyl ether) and molecular 5A (H_2, O_2, N_2, and CO) connected in series, using He as carrier gas. Each value of total conversion is the average of two different analyses taken after 3 h time-on-stream at a given temperature.

The hydrogen selectivity of the reaction was determined by comparing the molar hydrogen production rate to the maximum stoichiometrically allowable hydrogen production rate at a given methanol conversion (4).

$$S = \frac{r_{H2}}{3 r_{MeOH}} \qquad (4)$$

If the reaction is dominated by MSR, H_2, and CO_2 selectivities should lie at around 100%, whereas if methanol decomposition is the primary reaction, the H_2 selectivity lies at 67% and the CO_2 selectivity near zero.

3. Results and discussion

3.1. Properties of the HTlc precursor

PdZnAl, *PdMgGa* and *PdMgAl* HTlc precursors have been prepared with 1 mol% of the cations being Pd^{2+} and a $M^{2+}:M^{3+}$ ratio of 70:30 by co-precipitation. The XRD patterns of all as-synthesized precursor samples are typical of Hydrotalcite-like structure, as shown in Fig. 1. No Pd containing or other crystalline phases were observed. The crystallinity of the precursors decreased in the order of *PdMgGa* > *PdZnAl* > *PdMgAl* as indicated by the decreasing intensity as well as the increased peak broadening. The measured chemical
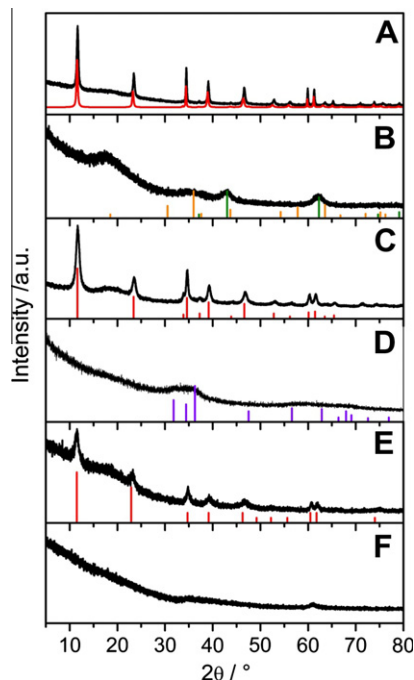
composition of Pd containing and Pd-free HTlc precursors is listed in Table 1. There are small deviations between the nominal and measured composition. In particular the M^{3+} content of *PdMgAl* and *PdMgGa* HTlc is increased to 35 mol% and the Pd content of *PdMgAl* HTlc is slightly higher than 1 mol% (1.3 mol%).

The specific surface areas of the HTlc precursor, as obtained by nitrogen physisorption, varied between 34 and 127 m^2/g (Table 1). The substitution of M^{2+} by Pd^{2+} resulted in an increase in the surface area in all samples probably due to hindered growth of the Pd-distorted HTlc lattice. In general, the surface area increases from *PdMgGa* < *PdZnAl* < *PdMgAl* which is in agreement with the broader XRD line profiles suggesting smaller crystallite size. Differences in surface area and XRD peak widths are compatible with the observation of SEM measurements. As shown in Fig. 2 the HTlc precursors show similar platelet-like morphology, but the particle sizes differed considerably. Small platelets were obtained for *PdMgAl* (Fig. 2C) and *PdZnAl* (Fig. 2A). The thickness of the platelets is in the low nanometer range, while the lateral dimension is approximately around 250 nm or below. Although for *PdMgAl* and *PdMgGa* samples the same synthesis conditions were applied the lateral size of the *PdMgGa* platelets is increased to 0.4–1 μm. The *PdMgGa* and *PdMgAl* platelets exhibit sandrose morphology, while the *Pd ZnAl* platelets are randomly oriented. However, no large Pd agglomerates were detected outside the platelets by SEM and also EDX mapping suggests a homogenous metal distribution for all samples (not shown).

3.2. Reducibility of the HTlc precursors and IMC formation

3.2.1. TPR and MS measurements

TPR experiments were performed in order to study the IMC formation and monitor the reduction process. All TPR profiles can be separated into three regions: a room temperature reduction (RTR), a low temperature reduction (LTR, <573 K) and high temperature reduction region (HTR, >573 K). RTR contains any initial hydrogen consumption detected upon switching to reducing atmosphere at room temperature before the heating ramp was started. Fig. 3 includes the LTR and HTR processes, only. The reduction from Pd^{2+} to metallic Pd^0 normally occurs in the RTR or LTR regime, at temperatures lower than ca. 423 K. Quantification of the degree of reduction from the hydrogen consumption turned out to be complex for these samples. Metallic Pd particles form hydrides and transfer spillover hydrogen to the support material; both phenomena lead to higher hydrogen consumption than expected for stoichiometric Pd^{2+} reduction [15]. The PdH_x phase is not stable during heating and decomposes at higher temperatures producing a negative peak in the TPR profile. In the HTR regime hydrogen consumption due to partial reduction of reducible metal oxides overlaps with further H_2 consumption due to conversion of CO_2, which is released as a decomposition product of the interlayer carbonate ions. As a matter of fact, CO and CH_4 have been detected by MS during LTR and HTR (Fig. 3, bottom). Thus, evolved CO_2 is not completely emitted from the catalyst bed, but varying fractions undergo rWGS and methanation at the surface of the metallic nanoparticles. This resulted in considerably higher hydrogen consumption than expected for stoichiometric reduction of the metal cations. Apparently, hydride formation, spillover hydrogen, and CO_2 conversion are dominating the consumption, and it is only considered in a semi-quantitative manner here, that is, by comparison of the TCD peak integrals of the different samples in the different temperature regimes.

As expected, no hydrogen consumption was observed in the RTR and LTR regions for the Pd-free samples. For the Pd containing precursors, the profiles in this region are different. RT and LT hydrogen consumption were observed for *PdMgGa* and *PdMgAl* samples, while for *PdZnAl* sample H_2 uptake was not detected at

Fig. 1. XRD patterns of (A) *PdMgGa* HTlc and simulated *MgGa* HTlc precursor; (B) ex-*PdMgGa* HTlc after reduction at 773 K, ICDD 1-1235 MgO (green), ICDD 10-113 $MgGa_2O_4$ (orange); (C) *PdZnAl* HTlc precursor and ICDD 38-486 $Zn_6Al_2(OH)_{16}\cdot CO_3\cdot 4H_2O$; (D) ex- *PdZnAl* HTlc after reduction at 523 K, ICDD 36-1451 ZnO (violet); (E) *PdMgAl* HTlc precursor and ICDD 14-191 $Mg_6Al_2(OH)_{16}CO_3\cdot 4H_2O$; (F) ex-*PdMgAl* HTlc after reduction at 523 K. (For interpretation of the references to color in this figure legend, the reader is referred to the web version of this article.)

Table 1
Chemical composition and textural properties of the HTlc precursor materials.

Sample	Measured composition[a] Pd:M^{2+}:M^{3+}	BET SA precursors (m^2/g)	BET SA reduced (m^2/g)	Pd content after reduction (wt.%)	Particle size by TEM (nm)
ZnAl	0:70.3:29.7	53	n.d.[b]	–	–
PdZnAl	1.0:69.5:29.5	85	86[c]	1.46	1.8[c]
MgGa	0:63.2:36.8	34	130	–	–
PdMgGa	1.0:64.5:34.5	48	116[d]	1.81	6.1[d]
MgAl	0:65.6:34.4	111	n.d.[b]	–	–
PdMgAl	1.3:69.1:29.6	127	123[c]	3.13	2.2[d]

[a] Determined by ICP-OES.
[b] n.d. = not determined.
[c] Reduced at 523 K.
[d] Reduced at 773 K.
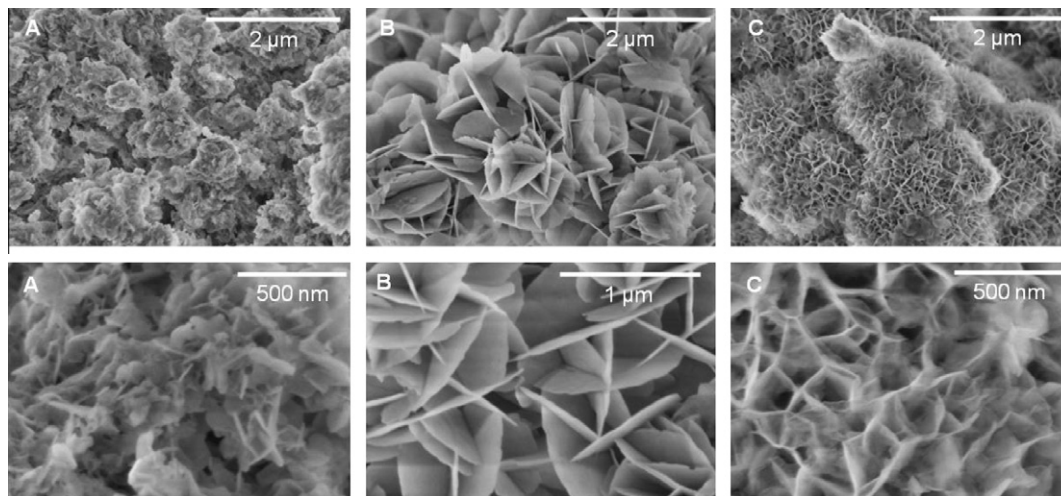
Fig. 2. SEM images of (A) *PdZnAl*, (B) *PdMgGa*, and (C) *PdMgAl* HTl precursor. (Bottom parts show magnification of top parts.)

RT. This suggests that in the former samples two different Pd^{2+} species were present, one easily and one harder to reduce. The main LTR peaks are found at 359, 382, and ca. 343 K for *PdZnAl*, *PdMgGa* and *PdMgAl*, respectively, which are relatively high values for the reduction of Pd^{2+}. From this observation, the RTR peak can be assigned reduction to PdO-like species not incorporated into the HTl lattice, while the LTR peaks are due to reduction of HTl-lattice Pd^{2+} cations. This assumption is consistent with XANES measurements discussed below. Furthermore, Pd hydride is observed only for the *PdMgAl* (small negative peak around 423 K). Additional LT hydrogen uptake was observed for *PdZnAl* at 520 K. It is known that ZnO can be reduced in the presence of Pd at such mild temperatures to form the IMC PdZn [13b,15]. Since the above-mentioned LTR peak is absent for the Pd-free precursor, it is assigned to reduction of ZnO with consequent IMC formation (although small amounts of CH$_4$ were detected at this temperature). No further peaks are detected in the LTR region for *PdMgGa* and *PdMgAl* samples. In *PdMgAl*, there are no other reducible species. In *PdMgGa*, this observation indicates that the IMC formation takes place at higher temperature. Therefore, the process cannot be accurately studied by TPR, because of the overlap with CO$_2$ conversion in the higher temperature regime, see Fig. 3 bottom.

In the HTR regime, hydrogen consumption was detected for all precursors, also for the Pd-free *MgGa* and *ZnAl*, except for *MgAl*. At these temperatures, partial reduction of the reducible oxides is expected also in the absence of Pd. Starting from *PdZnAl* and *ZnAl*, HTR consumption peaks having a similar integral area were observed at approximately same temperature (808 and 823 K). No MS-peaks of CO, or CH$_4$ were noticed at that temperature (Fig. 3). As a consequence, the peaks are assigned to reduction of the

ZnO-component of the support. For *MgGa* and *PdMgGa*, the presence of Pd leads to an increase in the total HTR hydrogen consumption and to a decrease in temperature from 736 to 695 K. In both samples, CO was detected by MS. Thus, at sufficiently high temperature CO$_2$ from decarboxylation of the interlayer carbonate anions undergoes rWGS on the reducible oxides [16]. In case of *PdMgGa* the hydrogen uptake due to rWGS and support reduction overlaps with IMC formation (Fig. 3). Only the non-reducible *MgAl* sample does not show any significant hydrogen consumption over the whole temperature range. Addition of Pd to this sample induced an uptake of hydrogen at 679 K; correspondingly, CH$_4$ was detected by MS (Fig. 3). Therefore, it is concluded that CO$_2$ deriving from decomposition of the interlayer carbonates is converted to methane over metallic Pd. TPR and MS data provide first evidence that the catalytic properties of Pd have been markedly modified by formation of IMCs. While *PdMgAl* (where no IMC is formed) was found to be active in methanation, *PdMgGa* converts CO$_2$ in the rWGS to CO at comparable conditions. The HTR hydrogen conversion of *PdZnAl* can be completely ascribed to the reducibility of the support material. From the TPR results, the reduction temperatures for IMC formation were estimated to 523 K for *PdZnAl* and 773 K for *PdMgGa*. The *PdMgAl* reference sample was reduced at 523 K.

3.2.2. XANES measurements

XANES measurements were carried out to gain more insight into the Pd speciation in the precursor and in the RTR and LTR events. Since TPR measurements suggested the presence of two Pd-species in *PdMgAl* and *PdMgGa*, different reference materials were used to evaluate the XANES data. Commercial PdO was chosen as reference material for segregated Pd^{2+} species in the
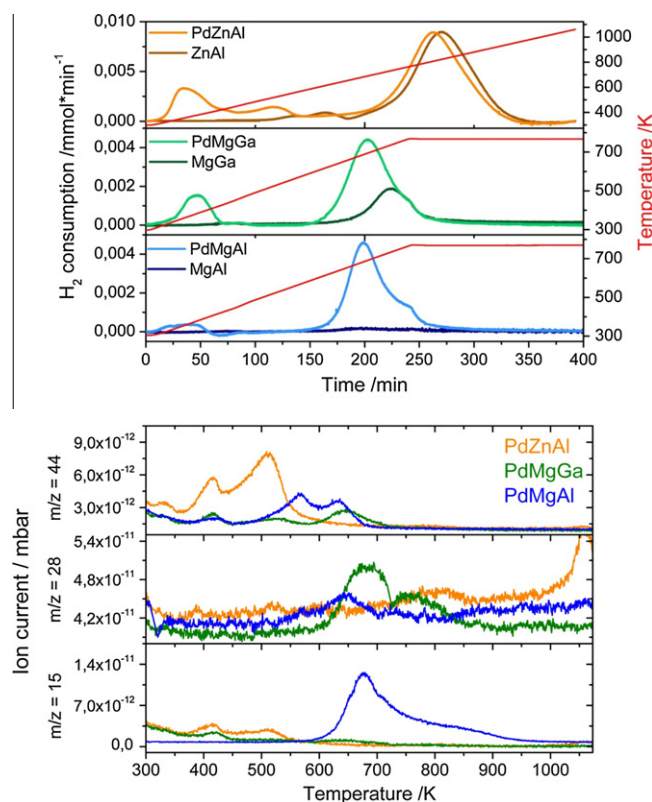
Fig. 3. TPR profiles of Pd substituted and unsubstituted Hydrotalcite-like precursors (top) and MS profiles (obtained by TGA-MS) in 5 vol% H_2/Ar (bottom).

precursor, which is not incorporated into the HTl lattice. Pd^{2+} in PdO prefers square planar coordination as well as Pd^{2+} in aqueous solution and most other solids. On the contrary, incorporation into the Hydrotalcite lattice requires octahedral coordination of Pd. The low-spin d^8 electronic configuration of Pd^{2+} makes regular octahedral coordination unstable with respect to large tetragonal elongations. Octahedral coordination of Pd^{2+} with oxygen was obtained in a high-pressure phase of PdO at 12 GPa [17]. Moreover, octahedral environment was also observed for Pd cations having higher oxidation states. For instance, Zn_2PdO_4 is a compound where Pd^{4+} has regular octahedral symmetry in the cubic spinel structure [18], while in $LaPdO_3$ Pd^{3+} has a distorted perovskite structure that stabilizes the trivalent ion in octahedral coordination [19]. The XANES spectra of the HTl precursors are shown in Fig. 4; both in the unreduced state and after treatment at 323 K in hydrogen, that is, at a temperature where RTR has already occurred, but low enough not to trigger LTR. XANES spectra of PdO as reference for segregated Pd^{2+} species before RTR and of metallic Pd for the state after RTR were included.

The intensity ratio of the white line and the first feature of the XANES spectrum of PdZnAl HTlc are significantly different from that of PdO. It is similar to that reported for $LaFe_{0.95}Pd_{0.05}O_3$ where Pd exhibits a distorted octahedral coordination and occupies Fe sites [20]. Changing to reducing atmosphere did not induce a change of the XANES of PdZnAl, which is in agreement with the TPR experiment that did not show any RT reduction. Therefore, we assume that in this sample Pd^{2+} is fully incorporated into the HTl structure and not available for reduction to metallic Pd below 323 K. Therefore, the PdZnAl spectrum recorded at RT in inert atmosphere was taken as a second reference for Pd^{2+} that is incorporated into the HT structure and exhibits octahedral coordination. Linear combination of PdO and PdZnAl spectra were used to obtain the fraction of Pd present as PdO and as incorporated within HT

structure, as shown in Fig. 4B and C. This analysis revealed that 68% of Pd^{2+} is present in octahedral coordination for PdMgGa, while in case of PdMgAl only 61% of Pd^{2+} is incorporated. Both samples showed a certain degree of RT reduction in the TPR (see Section 3.2.1). Accordingly, also the XANES spectra changed upon H_2 reduction at 323 K (Fig. 4). In particular for PdMgAl the near-edge features approach those of metallic Pd^0. The PdMgGa sample is apparently more stable and its XANES changes to a lesser extent. Still a significant shift of the second XANES feature to higher energy was observed also for this sample. This higher stability is in agreement with the higher LT reduction peak temperature compared with PdMgAl as observed in the TPR experiments (Fig. 3).

3.3. Properties of the ex-HTlc samples after reduction

The XRD patterns of the reduced samples presented in Fig. 1 contain only broad modulations of the background suggesting poor crystallinity and small crystallize sizes. After reduction at 523 K, PdMgAl is amorphous (Fig. 1F) and only heating to 773 K leads to significant growth of XRD peaks due to poorly crystalline MgO and $MgAl_2O_4$ (not shown). Formation of periclase and spinel phases was also observed for PdMgGa after reduction at 773 K (Fig. 1B). The PdZnAl sample showed very weak and broad peaks due to ZnO after reduction at 523 K (Fig. 1D). The XRD data are an agreement with HRTEM analysis of the phases of the support.

Because the metallic component was not able to be identified by means of XRD, probably due to the low total Pd content and the small crystallite size, XAFS and HRTEM were applied for phase identification. Fig. 5 shows the XANES spectra of the reduced precursors at the reduction temperatures deduced from the TPR experiment. Palladium foil, bulk Pd_2Ga and PdZn [21] are shown as reference materials. In general, lower amplitudes of the oscillations were observed in the XANES (Fig. 5) and EXAFS (Fig. 6) regions for the catalyst samples as a result of lower coordination number and/or higher disorder as expected for nanoparticles, in particular for PdZnAl, whose EXAFS spectra were too noisy to give reliable data. Nevertheless, the EXAFS spectra of the other catalysts and the XANES of all samples show resembled those of the associated bulk references regarding the features of the fine structure on the energy scale. This shows that the local environment around the Pd atoms and the bond distances to the neighboring atoms are similar in the nanocatalysts and the bulk references. In particular, good agreement was observed for the PdMgAl catalyst and the pure Pd reference, whereas there is a clear difference between Pd and the IMC catalysts confirming the modification of Pd by alloying and IMC formation.

TEM revealed that the platelet-like morphology of the HTlc precursor was retained after reduction and all catalysts showed spherical particles distributed on the platelets as presented in Figs. 7A and 8A. HRTEM images were used to determine the net plane distances and plane angles by FFT. Reduction of PdMgGa yielded well dispersed, supported nanoparticles as presented in Fig. 7A. The corresponding power spectrum of the HRTEM image, shown in Fig. 7B, allowed identification of the intermetallic Pd_2Ga phase (ICDD 65-1511). In agreement with XRD, partially crystalline MgO and $MgGa_2O_4$ were present as oxidic support [5]. However, for PdZnAl two different Pd-Zn IMCs were identified after reduction at 523 K. The crystal planes $(1\bar{1}1)$ and (111) of PdZn (ICDD 6-620) were identified with the characteristic acute angle of 65° along the $[\bar{1}01]$ zone axis (Fig. 8B and C). Differentiation of the closely related crystal structures of Pd and PdZn is often difficult by HRTEM as Pd particles produce similar patterns along the [1 1 0] zone axis, but the angle between the corresponding (octahedral) planes in the fcc Pd structure should be 70.5°. In several particles the lattice spacings d_{111} were systematically smaller than 0.22 nm, and d_{200} were larger than 0.20 nm, while in pure Pd (ICDD
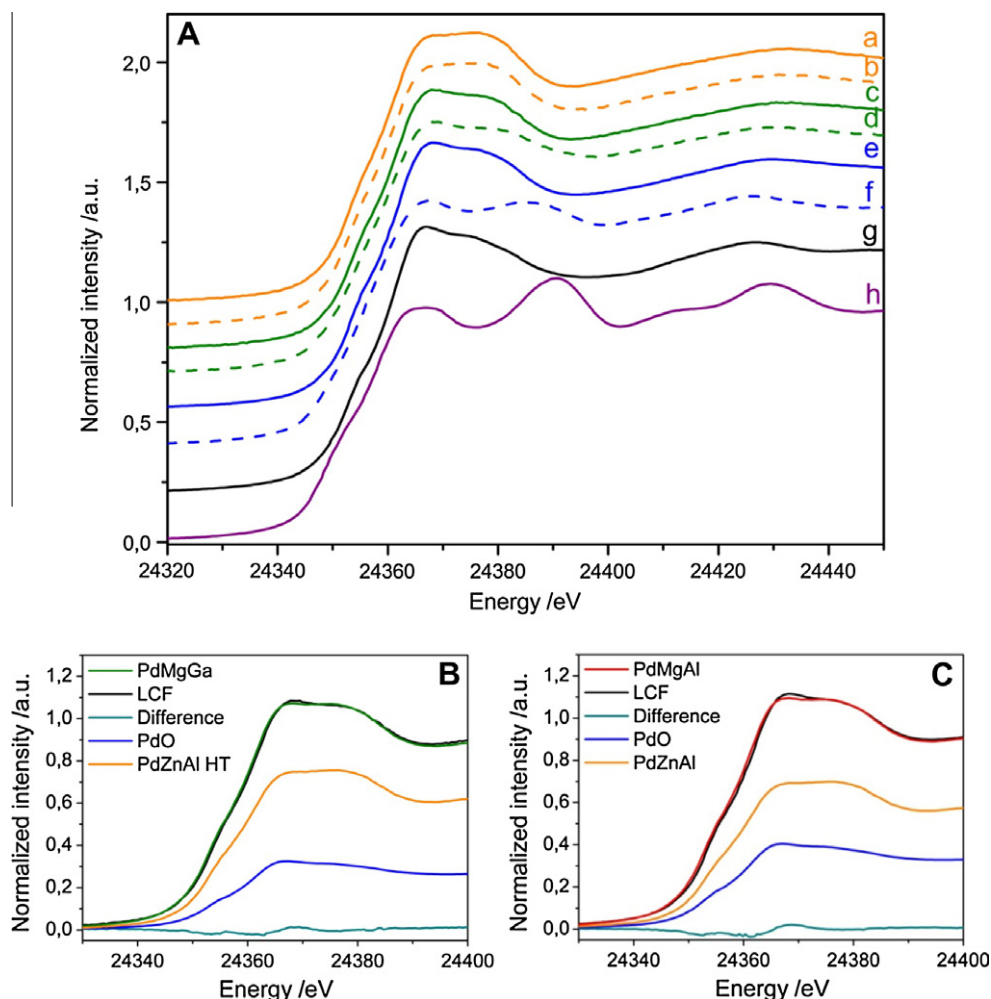
Fig. 4. (A) XANES spectra *PdZnAl* at RT/He (a) and 323 K/H$_2$ (b), *PdMgGa* at RT/He (c) and 323 K/H$_2$ (d), *PdMgAl* at RT/He (e) and 323 K/H$_2$ (f), PdO (g) and Pd foil (h) reference. (B and C) Linear combination fit of the XANES spectra of *PdMgGa* and *PdMgAl* precursor, by using PdO and *PdZnAl* as references for Pd^{2+} in square planar and octahedral coordination, respectively.

46-1043) d_{111} = 0.225 nm and d_{200} = 0.195 nm. Based on these differences the particles were identified as PdZn rather than Pd.

Additionally, nanoparticles with a core–shell structure were present. In one particle the phase in the core was identified as Pd$_2$Zn (circled area, ICDD 6-629) surrounded by an ordered shell of ZnO (Fig. 8E and F). This arrangement suggests that Pd$_2$Zn might be an intermediate of the reduction of *PdZnAl*. ZnO seems to have segregated from the oxide support to encapsulate the metal core by strong metal support interaction and supply further Zn atoms for IMC formation through the reactive Pd-ZnO and Pd$_2$Zn–ZnO interfaces, finally resulting in formation of PdZn. Fig. 9 shows the *PdMgAl* sample after reduction at 773 K. In STEM mode homogeneous and small-sized Pd nanoparticles on MgAlO$_x$ support were observed (Fig. 9A) and HRTEM investigations (Fig. 9B) confirming the presence of metallic Pd (ICDD 46-1043). The average particle sizes were obtained from projected areas of the metal particles and were 1.8, 2.2 and 6.1 nm for *PdZnAl* (based on 50 particles), *PdMgAl* (400 particles) and *PdMgGa* (1500 particles), respectively. The considerably larger size of the Pd$_2$Ga particles can be explained by higher reduction temperature that was necessary to form the IMC. The corresponding size distributions are shown in Fig. S2.

FT-IR spectroscopy of adsorbed CO was adopted to investigate the surface properties of the metallic Pd, PdZn and Pd$_2$Ga components in *PdMgAl*, *PdZnAl* and *PdMgGa* after reduction, respectively. The FT-IR spectra of CO adsorbed at room temperature on the three
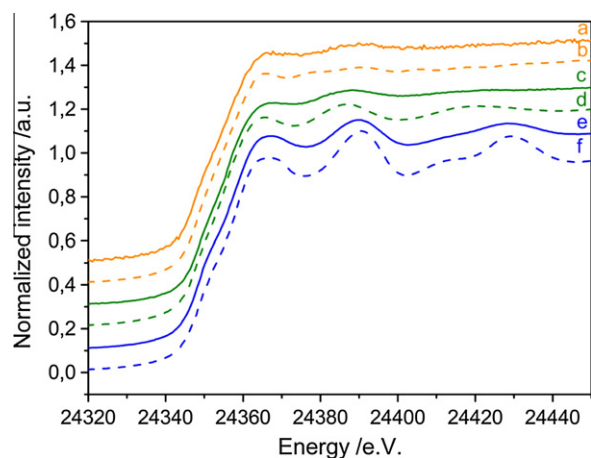

Fig. 5. In situ XANES spectra of (a) *PdZnAl* reduced at 523 K and (b) bulk PdZn, (c) *PdMgGa* reduced at 773 K, and (d) bulk Pd$_2$Ga, (e) *PdMgAl* reduced at 523 K and (f) Pd foil.

samples are shown in Fig. 10 as function of CO coverage. Several IR absorption bands were observed in the range of 2100–2000 cm^{-1} and 1970–1800 cm^{-1}. These bands are characteristic of linearly and multiply bonded CO on Pd^0 atoms, respectively [22]. As
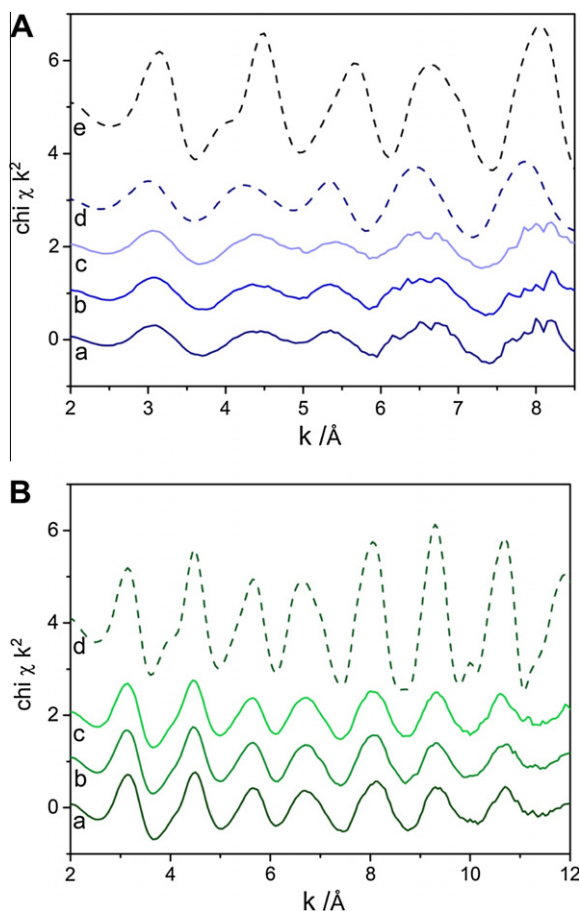
Fig. 6. Pd K edge EXAFS spectra (k^2 weighted) of *PdGaMg* (A) and *PdMgAl* (B) after reduction at 773 K (a), during MSR at 523 K (b), after 90 min MSR(c). Reference spectra are shown of bulk Pd_2Ga (d in A), and Pd foil (e in A and d in B).

2080 cm^{-1} gains intensity and slightly shifts to higher wavenumbers due to increased dipole–dipole coupling of the neighboring CO groups.

In summary, small metal particles have been obtained from HTlc precursors with at least partial Pd^{2+} incorporation on octahedral sites in the cationic layers. Upon reduction in hydrogen, elemental Pd segregated from the precursors at low temperature and as the reduction temperature increases, strong modification of the Pd phase are observed, which are attributed to the formation of IMC particles. Although the absence of remainders of elemental Pd in the IMC samples is hard to finally proof with each characterization method applied, the combination of imaging, bulk- and surface-sensitive techniques all provide evidence that Pd has reacted with the reducible oxide species in both samples. These results strongly suggest that the state of the freshly reduced samples is intermetallic. For *PdZnAl* the IMC PdZn is formed at 523 K probably via a Pd_2Zn intermediate stage. The average particle size is about 1.8 nm. Pd_2Ga formed from *PdMgGa* at higher temperature (773 K) and the average particle size is larger (6.1 nm). Compared with the monometallic Pd particles obtained by *PdMgAl*, the adsorptive properties of the IMC particles are strongly modified suggesting differences in catalytic properties.

3.4. Catalytic properties of the IMCs

3.4.1. Methanol synthesis from CO_2

Activity versus time-on-stream data for methanol synthesis and rWGS at 523 K is shown in Fig. 11 for all Pd-based catalysts. After a 5 h stabilization period, all catalysts show only very slow loss of activity with time-on-stream. *PdMgGa* and *PdZnAl* showed similar steady-state activities for methanol synthesis of 18.7 and 17.6 µmol/(g_{cat} min), respectively. These activities amounted to nearly 30 times the methanol synthesis activity of *PdMgAl* (0.65 µmol/(g_{cat} min)). In contrast to this difference, the rWGS of all catalysts were within a similar range, with *PdMgGa* (27.8 µmol/(g_{cat} min)) being twice as active as *PdMgAl* and *PdZnAl* with 14.3 and 13.5 µmol/(g_{cat} min), respectively. These results are consistent with those of Iwasa et al. [24] and Fujitani et al. [25], who showed that Pd supported on ZnO and Ga_2O_3 possessed significant methanol synthesis activity, whereas unsupported Pd and Pd on irreducible SiO_2 were almost inactive for methanol synthesis. Additionally, the results of Iwasa showed far less significant differences in rWGS rates on these catalysts. A similar observation about rWGS activities can be made for the catalysts studied in this work. From this observation it can be concluded that free Pd may be responsible for the rWGS activity, whereas the intermetallic sites lead to methanol formation. However, Iwasa et al. [24] had shown, that the rWGS activity of Pd/ZnO decreases by only 40% upon the complete conversion of Pd into a PdZn alloy. It is therefore possible that the intermetallic surfaces behave similarly to Cu, in that they possess sites for both methanol synthesis and rWGS.
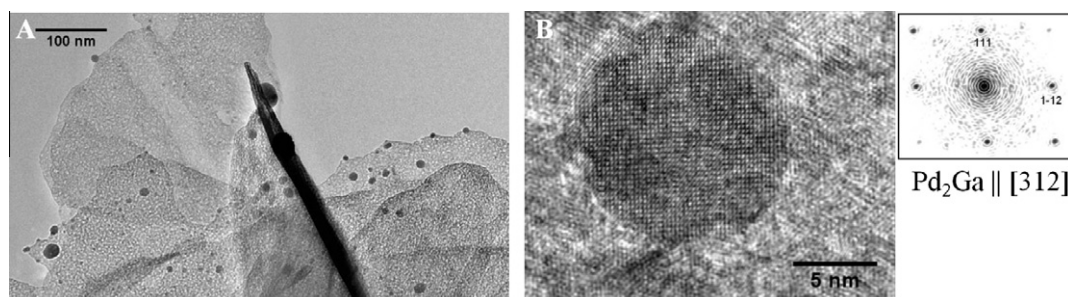
reported by Kovnir et al. [1] and Conant et al. [13c] the absence or strong reduction of multiple bonded carbonyl species should be observed for Ga–Pd and Pd–Zn intermetallic compounds. Indeed, mainly on-top coordinated CO species, characterized by IR absorption bands at 2080 cm^{-1} and 2050 cm^{-1} were observed for *PdMgGa* and *PdZnAl*, as shown in Fig. 10A and B. In contrast, CO absorption on *PdMgAl* sample revealed a much larger population of multiply bonded sites compared with linearly coordinated CO (Fig. 10C). At low CO coverage the band of linearly coordinated CO was observed at 2020 cm^{-1}, which is relatively low, but still in the characteristic range. According to Prinetto et al. [23] the frequency red shift originates from CO absorption on Pd sites, whose electronic properties are modified by interaction with basic support species. With increasing CO coverage, an additional band at

Fig. 7. (A) overview TEM images *PdMgGa* after reduction at 773 K in 5 vol% H_2/Ar and (B) HRTEM image and corresponding FFT pattern of Pd_2Ga.
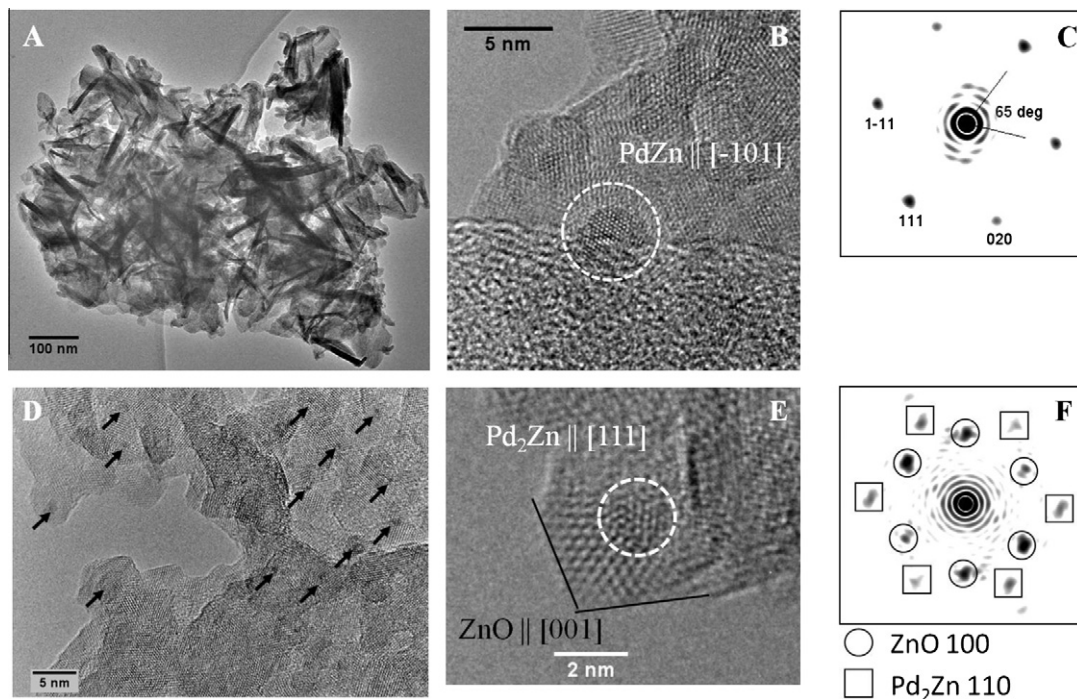
Fig. 8. (A and D) Overview TEM images, and (B and E) HRTEM and corresponding FFT pattern (C and F) of *PdZnAl* after reduction at 523 K in 5 vol% H$_2$/Ar.
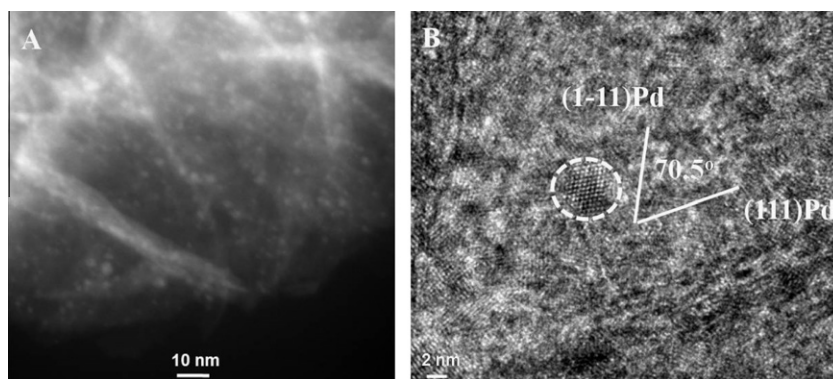

Fig. 9. (A) STEM and (B) HRTEM images of *PdMgAl* after reduction at 773 K in 5 vol% H$_2$/Ar.
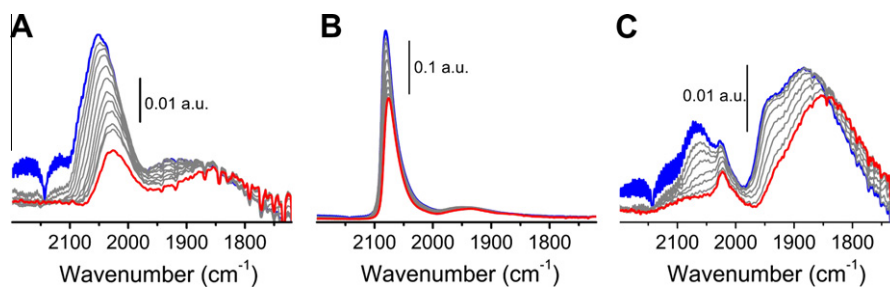

Fig. 10. FT-IR spectra of CO adsorbed at room temperature on (A) *PdZnAl* (reduced at 523 K), (B) *PdMgGa* (reduced at 823 K) and (C) *PdMgAl* (reduced at 523 K) as a function of CO coverage (θ_{max}: blue, θ_{min}: red). (For interpretation of the references to color in this figure legend, the reader is referred to the web version of this article.)

In order to compare the intrinsic activities and apparent activation energies for the Pd catalysts with those of a more active *CuZnAl* catalyst, which was also prepared from a single phase HTlc precursor, the space velocity had to be varied to reach similar conversion levels in the low-% range for all samples. *PdZnAl* shows a methanol selectivity of 60% and is more selective that *PdMgGa*

(47%), whereas the *CuZnAl* sample exhibits a higher selectivity of 82%. The methanol TOF of *CuZnAl* is 4–12 times higher than that of the IMCs (Table 2). The TOFs of the IMC catalysts in this work were estimated on basis of the average particle size as detected by TEM without consideration of possible variations in surface composition, segregation or particle embedment and thus are

likely afflicted with systematic errors. It should be noted, however, that the intrinsic activities of the IMCs are still two orders of magnitude higher than of *PdMgAl*.

The comparison of apparent activation energies between Cu- and Pd-based catalysts results in an intuitive understanding to the effect of IMC formation on reactivity. The Arrhenius plots for methanol synthesis and rWGS are shown in Fig. 11B for Pd-based catalysts tested at a space velocity of 10 mmol/(g_{cat} min) and *CuZnAl* at 93 mmol/(g_{cat} min). It is interesting to note that the activation energy for methanol synthesis decreases from 72 kJ/mol in *PdMgAl* to 68 kJ/mol in *PdZnAl* and 59 kJ/mol in *PdMgGa* upon the substitution of Al with Ga and Mg with Zn, respectively, and approaches 54 kJ/mol as measured for *CuZnAl*. Similarly for rWGS, substitution causes an increase in the apparent activation energy from 69 kJ/mol in *PdMgAl* to 94 kJ/mol and 82 kJ/mol for *PdZnAl*, *PdMgGa,* respectively, in the direction of *CuZnAl* (122 kJ/mol). The results suggest that the reactivity of Pd in methanol synthesis and rWGS approaches that of Cu upon substitution of irreducible species with Zn and Ga. In particular, these extraordinary differences in reactivity correspond to the formation of PdZn and Pd_2Ga IMCs upon reduction of *PdZnAl* and *PdMgGa,* respectively and the presence of only pure Pd upon reduction of *PdMgAl*, as evidenced by the aforementioned characterization results. The similarity of the catalytic properties of PdZn and Cu has been reported in literature and was attributed to the similar electronic structure. Both exhibit similar valence electron densities of states (DOS) as confirmed by DFT, UPS and XPS [26].

The fact that the catalytic properties do not evolve with the amount of "inert" species diluting the Pd metal atoms when going from pure Pd to the 2:1 IMC Pd_2Ga and further to the 1:1 IMC PdZn suggests that rather this modification of the electronic structure is responsible for the changes in activity and selectivity compared with a purely geometric site-isolation concept. The electronic structures depend on the crystal structures of the IMCs that differ from that of elemental Pd and are not subjected to continuous trends as expected for statistical fcc alloys, but need to be considered individually. Indeed, in case of Pd-Zn the Zn-poorer fcc alloy (α-phase) has recently been shown to exhibit catalytic properties greatly different from those of PdZn and to resemble rather those of elemental Pd [27].

3.4.2. Steam reforming of methanol

The catalytic activities of the Pd-based catalysts derived from HTlc precursors in MSR tests are summarized in Table 3. For all tested catalysts the main products were H_2, H_2O, CO and CO_2. Other reaction products such as formaldehyde or dimethylether were not observed. The *PdZnAl* and *PdMgGa* catalysts showed similar overall activity (9.5% methanol conversion), while the *PdMgAl* catalyst was somewhat less active (7% methanol conversion). The *PdZnAl* catalyst exhibited the highest hydrogen yield (660 μmol/ (g_{cat} min)) of all catalysts tested, and this hydrogen yield was 23% and 75% higher than those of *PdMgGa* and *PdMgAl*, respectively (Fig. 12). In terms of intrinsic activity for hydrogen production, the *PdZnAl* and *PdMgGa* were 2 and 6 times, respectively, more active than *PdMgAl*. The hydrogen selectivities of *PdMgGa* and *PdMgAl* were significantly lower (70%) than that of *PdZnAl* (87%). Although the monometallic Pd catalysts *PdMgAl* showed the lowest performance also in this reaction, the differences to the IMC catalysts in product yield and TOF are interestingly much smaller compared with the methanol synthesis tests. Marked differences are however seen in the selectivity toward CO_2.

While the reactivity of methanol on *PdMgAl* and *PdMgGa* is almost entirely dominated by methanol decomposition, *PdZnAl* shows considerable MSR activity with $S(CO)_2 = 61\%$. Iwasa et al. [11a] have attributed this CO_2 selectivity to the formation PdZn intermetallic phases during reduction of Pd/ZnO. However, the
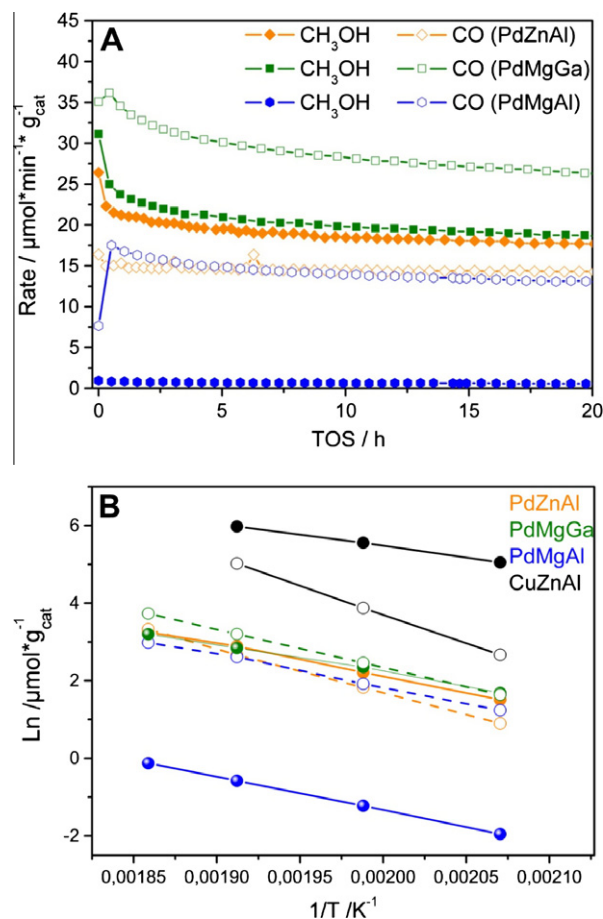

Fig. 11. (A) Rate of CO_2 hydrogenation over *PdZnAl*, *PdMgGa* and *PdMgAl* at 523 K (30 bar, 400 mg catalyst, 100 ml/min CO_2/H_2). (B) Arrhenius plot for methanol synthesis from CO_2 (closed symbols: MeOH, open symbol: CO).

CO_2 selectivities observed by Iwasa et al. were near 95% and thereby similar to those observed on *CuZn* based catalysts. Good activity and high CO_2 selectivity up to 99.4% and 98% were also reported for unsupported intermetallic bulk compounds [28] and aerosol-derived powders [2]. It should be noted that the particle size of the PdZn compounds observed by Iwasa et al. [11b], Friedrich et al. [28] and Halevi et al. [2] were far larger than the particles obtained in this work. It may therefore be possible that under reaction conditions the smaller particles decompose partially to yield metallic Pd, or that the methanol decomposition reaction is structure sensitive, and occurs faster on smaller particles. In accordance with the latter statement, Karim et al. [29], found a positive correlation between the number of small particles (<1.5 nm) and decreasing selectivity toward CO_2 on Pd/ZnO catalysts using TEM analysis.

Iwasa et al. [11b] and more recently, Haghofer et al. [12a] have shown that Pd supported on Ga_2O_3 is also very selective to MSR with CO_2 selectivities above 80%, and have attributed this high selectivity to the formation of Ga-Pd IMCs. However, for the *PdMgGa* sample investigated herein the CO_2 selectivity (16%) is only somewhat higher than that of the *PdMgAl* (6%) catalyst, in which no IMCs are formed. Haghofer et al. [14] have shown by in situ IR spectroscopy on Pd/Ga_2O_3 that the intermetallic Pd_2Ga surface is not entirely stable during MSR at 480 K, and that metallic Pd patches forms on the surface, as evidenced by the presence of bridge-bonded CO. At the higher temperatures (523 K) used in this study, such surface decomposition may occur to a greater extent and leave a higher fraction of exposed Pd, thus favoring methanol decomposition and leading to lower CO_2 selectivity.

Table 2
Activities for methanol synthesis from 1:3 CO_2:H_2 ratio at 30 bar on Pd-based and Cu-based catalysts at 523 K.

Catalyst	Metal site (μmol/g_{cat})	X_{CO2} (%)	Rate (μmol/min tg_{cat})		Space velocity (mmol/g_{cat} min)	S_{MeOH} (%)	TOF (min^{-1})	
			MeOH	CO			MeOH	CO
PdZnAl	73.4[a]	0.6	9.1	6.2	10	60	0.12	0.08
PdMgGa	20.4[a]	1.0	10.5	11.7	10	47	0.51	0.57
PdMgAl	90.9[a]	0.3	0.3	6.8	10	4	0.003	0.07
CuZnAl	170.9[b]	1.3	222.4	47.6	93	82	1.30	0.28

[a] Estimated from the metal particle size determined by TEM.
[b] Measured with N_2O reactive frontal chromatography.

Table 3
Activity results for the Pd-based IMC catalysts for the steam reforming of methanol at 523 K.

Catalyst	Metal sites[a] (μmol/g_{cat})	X_{MeOH} (%)	S_{CO2} (%)	Rate [μmol/min g]		S_{H2} (%)	TOF (min^{-1})	
				Methanol converted	H_2 released		MeOH	H_2
PdZnAl	73	14.0	61.1	369	964	87	5.1	13.2
PdMgGa	20	15.3	16.4	404	874	72	20.2	43.7
PdMgAl	91	12.6	6.1	331	681	69	3.6	7.5

[a] Estimated from the metal particle size determined by TEM.

Another aspect that deserves consideration is the difference in the interface of metallic and oxide phase due to the preparation technique applied in this study compared with most literature reports, where, for instance, well crystalline β-Ga_2O_3 has been used as support [11a,12a,12c]. In our samples the IMCs are supported on poorly crystalline MgO/$MgGa_2O_4$. The presence of the oxide component can influence the reactivity pattern in MSR [28,30] and also its nature should matter. However, in a study of Pd_2Ga particles of a similar size below 10 nm supported on crystalline β-Ga_2O_3 we have observed similar MSR properties as in this work [31]. This observation supports the hypothesis that the effect of particle size plays a more decisive role than the nature of the gallia-containing oxide support.

It should be noted that the promotional effect of Pd_2Ga formation on the selectivity is far more evident during methanol synthesis (as described previously) as compared to steam reforming. To that end, the higher hydrogen pressures and virtual absence of water during methanol synthesis may ensure the stability of the Pd_2Ga intermetallic surface responsible for the enhanced selectivity. In contrast, the presence of large concentrations of water during MSR may lead to a surface decomposition. Such a surface reaction can be expected to occur faster on small particles as studied in this work. However, the in situ EXAFS data (Fig. 6) do not show clear indications of decomposition and Pd segregation under

MSR conditions. It is thus concluded that such decomposition takes place only at the outer surface of the Pd_2Ga particles while the bulk remains in the IMC state. The product of the surface decomposition is not easily characterized and might be monometallic Pd or a Pd-rich alloy in addition to segregated Ga_2O_3. Corresponding to its lower formation temperature and the lower oxophilicity of Zn, the PdZn IMC seems to possess a greater stability in less reducing atmospheres than Pd_2Ga and the beneficial intrinsic catalytic properties observed in methanol synthesis prevail to a greater extent in the *PdZnAl* catalyst under wet MSR conditions. Still the same considerations about water-induced surface decomposition of the PdZn phase to unselective Pd or the α-Pd-Zn alloy [27] that might be accelerated by small and very reactive PdZn particles also hold in this system and are a likely explanation for the differences in performance observed between this and literature studies.

4. Conclusion

A flexible synthetic approach for the synthesis of nanoparticles of mono- and intermetallic compounds has been presented. Pd (2.2 nm), PdZn (1.8 nm), and Pd_2Ga (6.1 nm) nanoparticles were obtained from HTlc precursors with a homogeneous distribution of Pd and intimate interaction with the other reducible metal species. At a degree of substitution of 1 mol%, full incorporation of Pd^{2+} in the HTlc lattice has been confirmed for *PdZnAl*, while in *PdMgAl* and *PdMgGa* the majority of Pd^{2+} was incorporated. Upon reduction in hydrogen, metallic Pd segregated from the precursors at low temperature and for *PdZnAl* the IMC PdZn is formed at 523 K probably via a Pd_2Zn intermediate stage. Formation of Pd_2Ga IMC in *PdMgGa* requires 773 K. In comparison with the analogous *PdMgAl* sample, which does not contain a second reducible species and yields monometallic Pd nanoparticles, the CO absorption properties as well as the catalytic properties have markedly changed through formation of the IMCs. Improved activities and selectivities in MSR, and methanol synthesis from CO_2 have been observed. This effect is larger for CO_2 hydrogenation than for MSR. In the former reaction the Pd_2Ga-based catalyst showed the best performance, while the latter reaction is was the PdZn-based sample. These differences are probably related to the different sensitivity of the IMC surfaces against decomposition into Pd metal or a Pd-enriched bimetallic phase and oxide in the presence of water. The more reducing conditions of methanol synthesis seem to
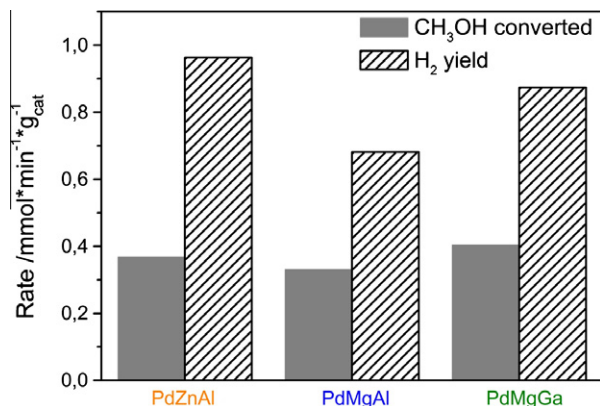
Fig. 12. Rate of MSR of *PdZnAl*, *PdMgGa* and *PdMgAl* catalysts in MSR conducted at 523 K.

stabilize the IMC better than the more oxidizing conditions of MSR. Under steady-state conditions, our Pd-based IMC catalysts are inferior to a Cu/ZnO reference system. Nevertheless, the potential of these materials for MSR operation at higher temperature and under changing reaction conditions like on–off operations remains to be investigated. The HTlc precursor approach has been shown as a valuable tool to investigate IMC catalysts in a nanostructured form and, in our future work, will be exploited for a deeper investigation of Pd-based IMCs and to explore different elemental combinations in comparative studies.

Acknowledgments

Appendix A. Supplementary data

Supplementary data associated with this article can be found, in the online version, at http://dx.doi.org/10.1016/j.jcat.2012.05.020.

References

[1] K. Kovnir, M. Armbrüster, D. Teschner, T.V. Venkov, F.C. Jentoft, A. Knop-Gericke, Y. Grin, R. Schlögl, Sci. Technol. Adv. Mater. 8 (2007) 420.
[2] B. Halevi, E.J. Peterson, A. DeLaRiva, E. Jeroro, V.M. Lebarbier, Y. Wang, J.M. Vohs, B. Kiefer, E. Kunkes, M. Havecker, M. Behrens, R. Schlögl, A.K. Datye, J. Phys. Chem. C 114 (2010) 17181.
[3] a X. Duan, D.G. Evans, Layered Double Hydroxides, Springer-Verlag, Berlin, Heidelberg, 2006;
b C. Forano, T. Hibino, F. Leroux, C. Taviot-Gueho, in: F. Bergaya, B.K.G. Theng, G. Lagaly (Eds.), Handbook of Clay Science, Elsevier, 2006, p. 1021.
[4] F. Cavani, F. Trifirò, A. Vaccari, Catal. Today 11 (1991) 173.
[5] A. Ota, M. Armbrüster, M. Behrens, D. Rosenthal, M. Friedrich, I. Kasatkin, F. Girgsdies, W. Zhang, R. Wagner, R. Schlögl, J. Phys. Chem. C 115 (2010) 1368.
[6] K. Kovnir, J. Osswald, M. Armbruster, D. Teschner, G. Weinberg, U. Wild, A. Knop-Gericke, T. Ressler, Y. Grin, R. Schlogl, J. Catal. 264 (2009) 93.
[7] G.A. Olah, A. Goeppert, G.K.S. Pakash, Beyond Oil and Gas: The Methanol Economy, Wiley-VCH Verlag GmbH & Co. KGaA, Weinheim, 2006.
[8] a R. Schlögl, Chemsuschem 3 (2010) 209;
b P.J. de Wild, M.J.F.M. Verhaak, Catal. Today 60 (2000) 3;
c F. Joensen, J.R. Rostrup-Nielsen, J. Power Sources 105 (2002) 195.
[9] R. Schögl, Energy Storage Materials, Walter de Gruyter, Berlin, 2012.
[10] L. Guczi, A. Erdôhelyi, Catalysis for Alternative Energy Generation, first ed., Springer, 2012.
[11] a N. Iwasa, S. Masuda, N. Ogawa, N. Takezawa, Appl. Catal. A 125 (1995) 145;
b N. Iwasa, T. Mayanagi, N. Ogawa, K. Sakata, N. Takezawa, Catal. Lett. 54 (1998) 119.
[12] a A. Haghofer, K. Föttinger, F. Girgsdies, D. Teschner, A. Knop-Gericke, R. Schlögl, G. Rupprechter, J. Catal. 286 (2012) 13;
b S. Penner, H. Lorenz, W. Jochum, M. Stöger-Pollach, D. Wang, C. Rameshan, B. Klötzer, Appl. Catal. A 358 (2009) 193;
c H. Lorenz, S. Penner, W. Jochum, C. Rameshan, B. Klötzer, Appl. Catal. A 358 (2009) 203.
[13] a C. Rameshan, W. Stadlmayr, C. Weilach, S. Penner, H. Lorenz, M. Hävecker, R. Blume, T. Rocha, D. Teschner, A. Knop-Gericke, R. Schlögl, N. Memmel, D. Zemlyanov, G. Rupprechter, B. Klötzer, Angew. Chem. Int. Ed. 49 (2010) 3224;
b K. Föttinger, J.A. van Bokhoven, M. Nachtegaal, G.n. Rupprechter, J. Phys. Chem. Lett. 2 (2011) 428;
c T. Conant, A.M. Karim, V. Lebarbier, Y. Wang, F. Girgsdies, R. Schlögl, A. Datye, J. Catal. 257 (2008) 64.
[14] M. Behrens, I. Kasatkin, S. Kühl, G. Weinberg, Chem. Mater. 22 (2009) 386.
[15] N. Iwasa, T. Mayanagi, W. Nomura, M. Arai, N. Takezawa, Appl. Catal. A 248 (2003) 153.
[16] W. Jochum, S. Penner, R. Kramer, K. Föttinger, G. Rupprechter, B. Klötzer, J. Catal. 256 (2008) 278.
[17] A.G. Christy, S.M. Clark, Phys. Rev. B 52 (1995) 9259.
[18] G. Demazeau, I. Omeran, M. Pouchard, P. Hagenmuller, Mater. Res. Bull. 11 (1976) 1449.
[19] S.-J. Kim, S. Lemaux, G. Demazeau, J.-Y. Kim, J.-H. Choy, J. Mater. Chem. 12 (2002) 995.
[20] A. Eyssler, P. Mandaliev, A. Winkler, P. Hug, O. Safonova, R. Figi, A. Weidenkaff, D. Ferri, J. Phys. Chem. C 114 (2010) 4584.
[21] M. Friedrich, A. Ormeci, Y. Grin, M. Armbruster, Z. Anorg. Allg. Chem. 636 (2010) 1735.
[22] N. Sheppard, C. De La Cruz, Catal. Today 70 (2001) 3.
[23] F. Prinetto, M. Manzoli, G. Ghiotti, M.d.J. Martinez Ortiz, D. Tichit, B. Coq, J. Catal. 222 (2004) 238.
[24] N. Iwasa, H. Suzuki, M. Terashita, M. Arai, N. Takezawa, Catal. Lett. 96 (2004) 75.
[25] T. Fujitani, M. Saito, Y. Kanai, T. Watanabe, J. Nakamura, T. Uchijima, Appl. Catal. A 125 (1995) L199.
[26] a A.P. Tsai, S. Kameoka, Y. Ishii, J. Phys. Soc. Jpn. 73 (2004) 3270;
b A. Bayer, K. Flechtner, R. Denecke, H.-P. Steinrück, K.M. Neyman, N. Rösch, Surf. Sci. 600 (2006) 78;
c K.M. Neyman, K.H. Lim, Z.-X. Chen, L.V. Moskaleva, A. Bayer, A. Reindl, D. Borgmann, R. Denecke, H.-P. Steinrück, N. Rösch, Phys. Chem. Chem. Phys. 9 (2007) 3470;
d Z.-X. Chen, K.M. Neyman, A.B. Gordienko, N. Rösch, Phys. Rev. B 68 (2003) 075417.
[27] B. Halevi, E.J. Peterson, A. Roy, A. DeLariva, E. Jeroro, F. Gao, Y. Wang, J.M. Vohs, B. Kiefer, E. Kunkes, M. Hävecker, M. Behrens, R. Schlögl, A.K. Datye, J. Catal.
[28] M. Friedrich, D. Teschner, A. Knop-Gericke, M. Armbrüster, J. Catal. 285 (2012) 41.
[29] A. Karim, T. Conant, A. Datye, J. Catal. 243 (2006) 420.
[30] C. Rameshan, W. Stadlmayr, S. Penner, H. Lorenz, N. Memmel, M. Hävecker, R. Blume, D. Teschner, T. Rocha, D. Zemlyanov, A. Knop-Gericke, R. Schlögl, B. Klötzer, Angew. Chem. Int. Ed. 51 (2012) 3002.
[31] L. Li, B. Zhang, E. Kunkes, K. Föttinger, M. Armbrüster, D. Sheng Su, W. Wei, R. Schlögl, M. Behrens, ChemCatChem, htttp://dx.doi.org10.1002/cctc.201200268.